

Recollimation shocks in the relativistic outflows of active galactic nuclei

Doctoral Thesis Award Lecture 2014

C. M. Fromm*

Max-Planck-Institut für Radioastronomie, Auf dem Hügel 69, 53121 Bonn, Germany

Received 2015 Mar 31, accepted 2015 Apr 7

Published online 2015 Jun 22

Key words galaxies: active – galaxies: jets – quasars: individual (CTA 102) – radio continuum: galaxies – radiation mechanism: non-thermal

We analysed the single-dish radio light curves of the blazar CTA 102 during its major flare around April 2006. The modelling of these data revealed a possible travelling shock–recollimation shock interaction during the flare. To verify this hypothesis, we used multi-epoch and multi-frequency very-long baseline interferometry (VLBI) observations and performed a detailed kinematic and spectral analysis. The results confirmed the hypothesis of a shock-shock interaction causing the 2006 radio flare and provided indications for additional recollimation shocks farther downstream.

© 2015 WILEY-VCH Verlag GmbH & Co. KGaA, Weinheim

1 Introduction

The jets in Active Galactic Nuclei (AGN) are among the most powerful objects in the universe. They are launched in the direct vicinity of supermassive black holes (SMBH) located in the centres of galaxies. They show spectral variations throughout the entire electro-magnetic spectrum from the radio to γ -ray regime and exhibit a plasma travelling nearly at the speed of light. Blazars are a subclass of AGNs seen under small viewing angles, $\vartheta < 5^\circ$ and are famous for the appearance of superluminal motion, a special relativistic effect due to the plasma velocities close to the speed of light and the small viewing angle.

The blazar CTA 102 is located at a redshift $z = 1.037$ (luminosity distance, $D_L = 6.4$ Gpc) and was first observed by Harris & Roberts (1960). The kilo-parsec scale structure of the source shows a central core and two faint lobes separated by roughly $2.6''$ (Spencer et al. 1989). The parsec-scale structure of the jet in CTA 102 is resolved by VLBI observations allowing us to trace regions of enhanced brightness, commonly referred as component, over several years. Those observations reveal a bent jet with several regions of enhanced emission and superluminal motions up to twelve times the speed of light (Lister et al. 2009). The flaring activity in AGNs can be connected to the appearance of new traveling components close to the observed onset of the radio jet, the so-called radio core (see, e.g., Marscher et al. 2008, 2010).

During April 2006, CTA102 underwent a major flare that was observed via single-dish observations from the cm- to the mm-wavelength and via VLBI observations at different frequencies, including a set of eight simultane-

ous multi-frequency observations from 2 GHz to 86 GHz (Fromm et al. 2011, 2013a,b). In this paper we present a summary of the analysis of the single dish and VLBI observations during the 2006 radio flare in CTA 102 and a possible interpretation of the data via shock-shock interaction close to the radio core.

The organization of the paper is the following: In Sect. 2 and Sect. 3, we present the used single-dish and multi-frequency VLBI observations, and their analysis is shown in Sect. 4. The interpretation and discussion of the results can be found in Sect. 5, and the conclusions are provided in Sect. 6. Throughout the paper we define the spectral index, α , using the relation $S_\nu \propto \nu^\alpha$. The optically thin spectral index, α_0 , can be derived from the spectral slope, s , of the relativistic electron distribution ($N \propto E^{-s}$), via the relation $\alpha_0 = -(s - 1)/2$. We define the optically thin spectral index as $\alpha_0 < 0$. We adopt the following cosmological parameters: $\Omega_m = 0.27$, $\Omega_\Lambda = 0.73$, and $H_0 = 71 \text{ km s}^{-1} \text{ Mpc}^{-1}$. This results in a linear scale of 8.11 pc mas^{-1} or $26.45 \text{ ly mas}^{-1}$ for CTA 102 ($z = 1.037$). With these conventions, 1 mas yr^{-1} corresponds to $52.9 c$. We use R for the radius of the jet and r for the distance along the jet.

2 Single-dish observations

CTA 102 is observed on a regular basis with the Radio Observatory of the University of Michigan (UMRAO), the Metsähovi Radio Observatory and the Sub-Millimetre Array (SMA). In Table 1 we present a summary of the observing frequencies and the typical time sampling of the light curves, and in Fig. 1 we show the single-dish light curve of CTA 102 at various frequencies between 2004 and 2010.

* Corresponding author: cfromm@mpifr.de

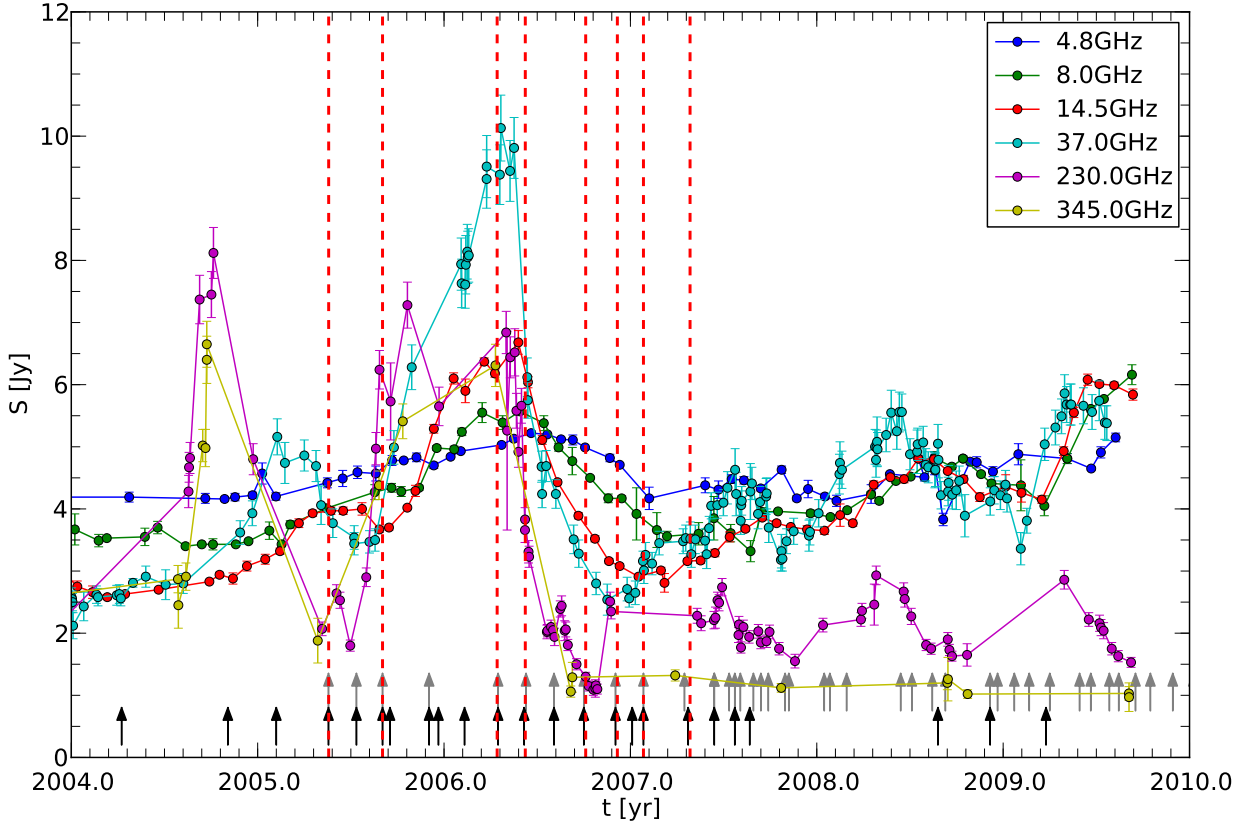


Fig. 1 Single-dish light curve of the blazar CTA 102 centred around the 2006 radio flare. The vertical dashed lines correspond to multi-frequency VLBI epochs and the black and grey arrows indicate the epochs for 15 GHz and 43 GHz VLBI observations.

The radio flare around 2006.0 is the most prominent feature in the light curve (clearly visible at 37 GHz) and is surrounded by a smaller high-frequency flare in 2004.8 and smaller flares prior to the major one. The 2006 radio outburst shows the typical evolution of the flare: It starts at high frequencies, and the peak flux density is shifted towards lower frequencies with time. This so-called time delay is clearly visible at all frequencies (see Fig. 1).

In order to perform a spectral analysis we interpolated the single dish light curves using an adequate time sampling (for details on the interpolation, see Fromm et al. 2011) and fitted a synchrotron self-absorbed spectrum to each spectra. The synchrotron self-absorbed spectrum is characterised by the turnover flux density, S_m , the turnover frequency, ν_m , and the optically thin and thick spectral indices, α_0 and α_t :

$$S_\nu = S_m \left(\frac{\nu}{\nu_m} \right)^{\alpha_t} \times \frac{1 - \exp\left(-\tau_m (\nu/\nu_m)^{\alpha_0 - \alpha_t}\right)}{1 - \exp(-\tau_m)}, \quad (1)$$

where $\tau_m \approx 3/2 \left(\sqrt{1 - \frac{8\alpha_0}{3\alpha_t}} - 1 \right)$ is the optical depth at the turnover frequency.

Since the observed spectrum during the flare may in general be thought as the superposition of the emission of the steady and perturbed jet, we have to reconstruct the emission from the steady (quiescent jet). Therefore, we used archival data and extracted the minimum flux density (around $t = 1989$) from the low frequency curves

Table 1 Observing frequencies and average time sampling for the used light curves.

Observatory	ν [GHz]	$\langle t_{\text{obs}} \rangle$ [d]
UMRAO	4.8	46
UMRAO	8.0	38
UMRAO	14.5	32
Metsähovi	37	16
SMA	230	27
SMA	340	132

(4.8–37 GHz). We applied a power law $S(\nu) = c_q \nu^{\alpha_q}$ to the data and obtained $c_q = 7.43 \pm 0.65 \text{ Jy GHz}^{-1}$ and a spectral index $\alpha_q = -0.45 \pm 0.04$. During the fitting process we removed the contribution of the quiescent spectrum to obtain the flaring spectrum. In Fig. 2 we present the result of the spectral fitting for the 2006.20 data.

The evolution of the 2006 radio flare in the turnover frequency–turnover flux density plane can be seen in Fig. 3 (for details on the fitting process and the error analysis, see Fromm et al. 2011). The flare was first detected at high turnover frequency ($\nu_m \sim 200$ GHz) and low turnover flux density ($S_m \sim 3$ Jy). During the first 0.2 yr of the flare the turnover flux density increased while the turnover frequency decreased reaching a peak at $\nu_m \sim 110$ GHz and $S_m \sim 8.5$ Jy around 2005.8. After passing this peak, both,

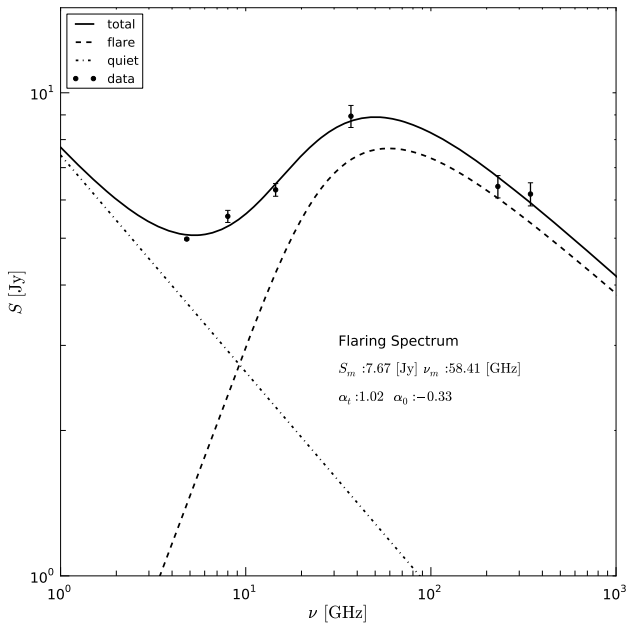


Fig. 2 Result of the spectral fitting to the 2006.20 data. The dashed-dotted line corresponds to the quiescent spectrum, the dashed line to the flaring spectrum, and the solid black line to the total spectrum. The values presented indicate the spectral turnover of the flaring spectrum.

the turnover flux density and the turnover frequency decreased, reaching a local minimum around 2006.0, followed by an additional increase in the turnover flux density leading to second peak around 2006.3 with $\nu_m \sim 56$ GHz and $S_m \sim 8.4$ Jy. This second peak was followed by a continuous decrease in the turnover flux density and the turnover frequency until the end of the flare in 2006.8.

3 VLBI observations

VLBI observations provide the unique capability of resolving the structure of relativistic jets and can be used to investigate the temporal and spatial variations of the emission and the underlying plasma flow. We included in our data set on CTA 102 several archival single-epoch (15 GHz and 43 GHz) and simultaneous multi-frequency (2 GHz – 86 GHz) VLBI observations (see Fig. 1 and Fromm et al. 2013a for details on the VLBI observations). The 15 GHz VLBI observations were taken from the MOJAVE¹ archive and the 43 GHz VLBI observations from the Boston University Blazar Monitoring². In total, our data set consists of thirty-six 15 GHz, fifty-eight 43 GHz, and eight multi-frequency VLBI observations.

For the calibration of the data, we used the National Radio Astronomy Observatory's (NRAO) Astronomical Image Processing System (AIPS), and the fully calibrated

¹ Monitoring of Jets in Active galactic nuclei with VLBA Experiments <http://www.physics.purdue.edu/MOJAVE>

² <http://www.bu.edu/blazars/research.html>

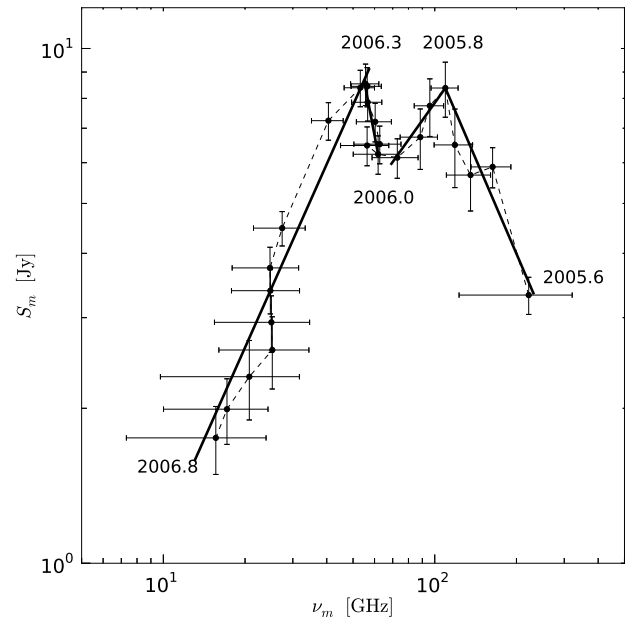


Fig. 3 The evolution of the 2006 radio flare in the turnover frequency–turnover flux density (ν_m - S_m) plane. The temporal evolution of the flare is indicated by the time labels. The black solid line corresponds to a model using the modified shock-in-jet model (see Sect. 4.1 for details).

data were exported into DIFMAP (Shepherd 1997). For imaging and model fitting of the observations we used the CLEAN algorithm combined with phase and amplitude self-calibration and MODELFIT algorithms. We fitted circular Gaussians (in the following referred to as components), characterised by their flux density, their position (radius and position angle) and their FWHM, to the calibrated images in order to trace the evolution of the flux density along the jet (Fromm et al. 2013a,b). These components can be cross-identified from epoch to epoch and thus their velocity and/or ejection epoch can be computed.

Simultaneous multi-frequency VLBI observations allow us to study the same physical region within the jet at different angular resolution. As already mentioned in Sect. 2, the synchrotron spectrum is characterised by the turnover frequency, ν_m , and turnover flux density, S_m . If the observing frequency is smaller than ν_m the emission is self-absorbed (optically thick). In contrast, if the observing frequency is higher than the turnover frequency, the emission is optically thin. This transition depends on the physical properties of the jet, e.g., the magnetic field and particle density ($\nu_m \propto B^{(s+2)/(s+4)}$). Therefore, this transition typically occurs at the observed onset of the jet, the so-called core. This effect together with the increased angular resolution is reflected in the multi-frequency VLBI observations by the splitting of the core region into several components with increasing frequency. For labelling the fitted components, we use capital letters for the same physical regions and the numbers increase with decreasing core distance.

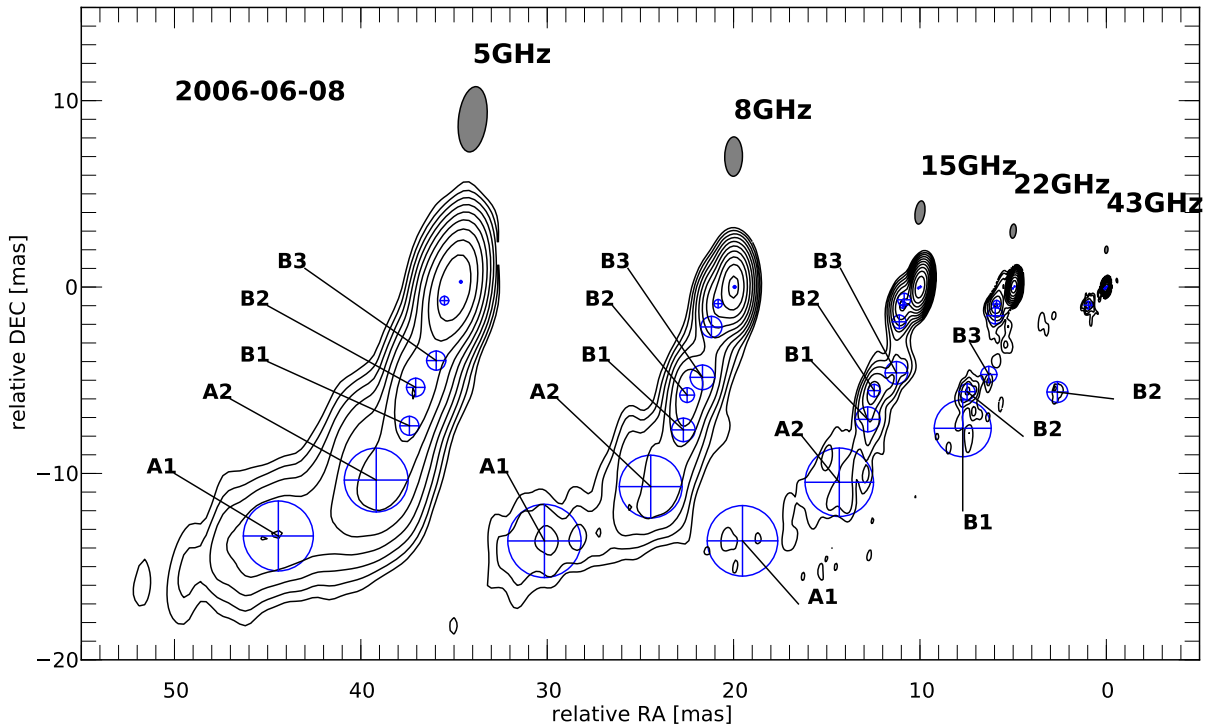


Fig. 4 Uniform weighted VLBA CLEAN images with fitted circular Gaussian components at different frequencies for the July 2006 observation of CTA102. The lowest contour is plotted at 10 times the off-source rms at 43 GHz and increases in steps of 2. The observing frequency and the restoring beam size are plotted above each map. For the labeling we use capital letters for the same physical region in the jet, and the numbers increase with inverse distance from the core. For a more detailed picture of the core region see Fig. 5.

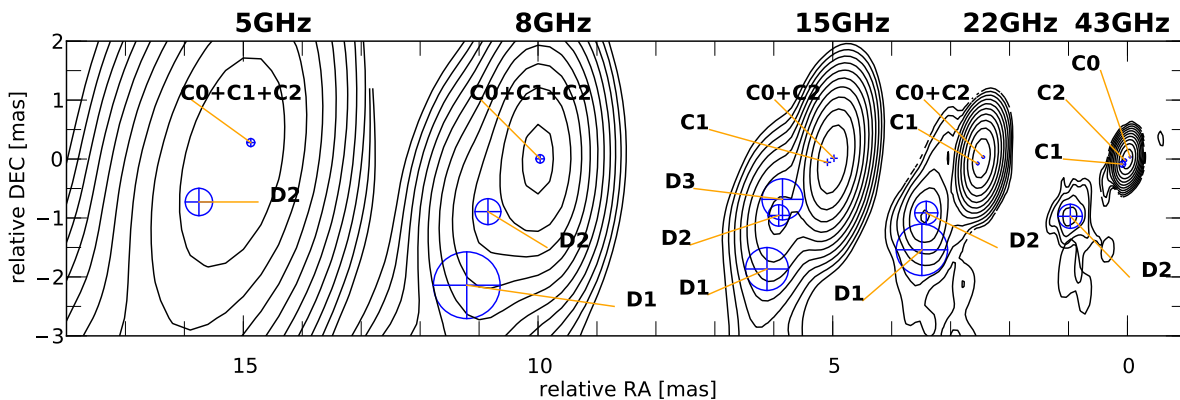


Fig. 5 Zoom into the core region for the images presented in Fig. 4 corresponding to epoch 2006-06-08, showing the splitting of the C-components with increasing frequency. For map details see the caption of Fig. 4.

In Fig. 4 we show the full-calibrated multi-frequency VLBI images of CTA 102 with cross-frequency identified fitted components for the June 2006 observations. The splitting of the core region in several components with increasing frequency is presented in Fig. 5.

4 Modelling

4.1 Shock-in-jet model

The shock-in-jet model is often used to describe the evolution of flares in relativistic jets. This model assumes a shock

wave travelling through a steady state jet. At the shock front, particles are swept up and gain energy via shock acceleration in a small layer behind the shock front. The width of this layer depends on the dominant energy loss mechanisms, e.g., Compton, synchrotron and adiabatic losses. The standard evolution of flares according to the shock-in-jet model consists of three stages, namely: the rise of flare, dominated by Compton losses (increasing S_m while ν_m is decreasing), a second stage where synchrotron losses are the main energy loss mechanism (nearly constant S_m while ν_m decreases) and finally the adiabatic stage, where adiabatic, i.e., expan-

sion losses, are the most important energy losses (both, S_m and ν_m decrease; Marscher & Gear 1985).

The model assumes a power law distribution of relativistic electrons, $N(E) = KE^{-s}$ with normalisation coefficient K . If the jet radius, R , follows a power law with distance along the jet, $R \propto r^\rho$, the evolution of the normalisation coefficient, K , the magnetic field, B , and the Doppler factor, D , can be written as power laws (Marscher & Gear 1985; Türler et al. 2000):

$$K \propto r^{-\rho b}, \quad B \propto r^{-\rho b}, \quad D \propto r^{-\rho d}. \quad (2)$$

Using the theory of synchrotron emission and taking into account Compton, synchrotron, and adiabatic losses, the evolution of the turnover frequency, ν_m , and turnover flux density, S_m , can be written as power laws (Fromm et al. 2011; Türler et al. 2000):

$$\nu_m \propto t^{n_i/\xi}, \quad (3)$$

$$S_m \propto t^{f_i/\xi}, \quad (4)$$

where $\xi = (2\rho d + 1)/\rho$. The exponents n_i and f_i are defined as

$$n_1 = \frac{-(b+1)/4 - d(s+3)}{(s+5)}, \quad (5)$$

$$n_2 = \frac{-[2k + b(s-1) + d(s+3)]}{(s+5)}, \quad (6)$$

$$n_3 = \frac{-[2(k-1) + (b+d)(s+2)]}{(s+4)}, \quad (7)$$

$$f_1 = \frac{(11-b)/8 - d(3s+10)}{(s+5)}, \quad (8)$$

$$f_2 = \frac{2 - [5k + b(2s-5) + d(3s+10)]}{(s+5)}, \quad (9)$$

$$f_3 = \frac{[2s + 13 - 5k - b(2s+3) - d(3s+7)]}{(s+4)}, \quad (10)$$

$$(11)$$

where $i = 1$ corresponds to the stage dominated by Compton losses, $i = 2$ to synchrotron losses, and $i = 3$ to adiabatic losses (for details of the model and derivation of the equations see, e.g., Fromm et al. 2011).

We applied the shock-in-jet model to the extracted turnover flux densities and turnover frequencies during the 2006 radio flare in order to obtain the evolution of the underlying physical properties of the jet. Notice that the double hump structure in the ν_m - S_m plane can not be fitted with the standard 3-stage evolution (Compton, synchrotron and adiabatic stage). Therefore, we included a second Compton stage in the model which allowed us to fit the obtained spectral evolution of the 2006 radio flare. In Table 2 and Fig. 3 we present the results for the modelling of the spectral evolution in CTA 102 during the 2006 radio flare (for more details on the fitting and error analysis, see Fromm et al. 2011).

4.2 VLBI kinematics

Throughout our VLBI data set we could cross-identify (across epochs and frequencies) seven components. Due to

Table 2 Best-fit values for spectral evolution modeling of the 2006 radio flare in CTA 102 for the parameters b , d , s , k , and r .

	2005.60–2005.95 Compton-Adiabatic	2005.95–2006.30 Compton	2006.3–2006.8 Adiabatic
b	$1.0_a^{+0.08}$	$1.35_{-0.35}^{+0.65}$	1.7 ± 0.2
d	0.2 ± 0.02	-0.1 ± 0.03	$-0.2_{-0.05}^{+0.08}$
s	2.1	2.0	2.4
k	2.7 ± 0.14	not fitted	4.7 ± 0.4
ρ	0.60 ± 0.03	0.35 ± 0.02	0.90 ± 0.07

^a Value hits lower boundary.

the increase of angular resolution with frequency and self-absorption effects, the cross-identification of components in the core region was difficult, but we detected four components within the first 0.6 mas using the 43 GHz VLBI observation.

We fitted polynomials to the obtained x and y coordinates of the components in order to derive the kinematics, i.e., angular speed, apparent speed, Doppler factor, and ejection epoch. We followed Homan et al. (2001) and Schinzel et al. (2012), using first- and second-order polynomials if the component was detected in more than ten epochs, the latter can only be applied to the long-term monitoring of the source at 15 GHz and 43 GHz):

$$x(t) = \mu_x (t - t_{x,0}) + \frac{\dot{\mu}_x}{2} (t - t_{\text{mid}})^2, \quad (12)$$

$$y(t) = \mu_y (t - t_{y,0}) + \frac{\dot{\mu}_y}{2} (t - t_{\text{mid}})^2, \quad (13)$$

where $\mu_{x,y}$ is the angular speed, $t_{\text{mid}} = (t_{\text{min}} + t_{\text{max}})/2$ with $t_{\text{min,max}}$ are the epoch of first and last detection of the component, $t_{x,0} = t_{\text{mid}} - x(t_{\text{mid}})/\mu_x$ and $t_{y,0} = t_{\text{mid}} - y(t_{\text{mid}})/\mu_y$ are the component ejection times. The ejection epoch can only be calculated for clearly radial outward moving features by a simple back interpolation of the trajectory. Using the average angular speed $\langle \mu \rangle$ obtained, we computed the apparent speed, β_{app} , and the Doppler factor, δ . The apparent speed of the components, β_{app} , is derived from the angular speed, μ , as

$$\beta_{\text{app}} = \frac{\langle \mu \rangle D_L}{1+z}, \quad (14)$$

where D_L is the luminosity distance and z the redshift. We computed the Doppler factor assuming that the jet is seen under the critical viewing angle, ϑ_{crit} , which can be derived by calculating the derivative of the apparent speed $\beta_{\text{app}} = \beta \sin \vartheta / (1 - \beta \cos \vartheta)$ with respect to ϑ for any given β . This leads to the result that the maximum apparent speed is obtained if $\cos \vartheta_{\text{crit}} = \beta = [\beta_{\text{app}}^2 / (1 + \beta_{\text{app}}^2)]^{1/2}$. For jets seen at this critical angle, the Doppler factor is $\delta_{\text{crit}} = \sqrt{1 + \beta_{\text{app}}^2}$.

In the following, we shortly describe the kinematics of the cross-identified components. A summary of the kinematic parameters can be found in Table 3. For a more de-

Table 3 Results of the kinematic analysis for the cross-identified components.

Comp.	$\langle\mu\rangle$ [mas yr ⁻¹]	β_{app} [c]	δ_{crit} [1]	ϑ_{crit} [°]	t_{ej} [yr]	$\langle r \rangle$ [mas]	acc	Notes
A1	0.18±0.03	9.4±1.9	9	6	–	17.0±0.5	no	no-radial inward
A2	0.17±0.01	8.7±0.5	9	7	1945±6	11.2±0.2	no	radial outward
B1	0.016±0.005	0.85±0.25	1	–	–	7.6±0.3	yes	no-radial outward
B2	0.015±0.003	0.77±0.14	1	–	–	6.2±0.1	no	radial inward
B3	0.027±0.006	1.41±0.32	2	–	–	5.1±0.2	no	non-radial outward
D1	0.10±0.02	5.7±1.2	6	10	–	2.1±0.4	yes	non-radial outward
D2	0.16±0.01	8.3±0.6	8	7	1997.1±0.4	1.6±0.4	yes	radial outward
C1	0.22±0.06	11.6±3.0	12	5	2005.1±0.2	0.2±0.1	no	radial outward
C2	0.25±0.04	13.0±2.1	13	4	2005.9±0.2	0.4±0.2	no	radial outward
C3	0.07±0.01	3.8±0.6	4	15	–	0.2±0.1	yes	non-radial outward
C4	0.17±0.01	9.1±0.5	9	6	–	0.2±0.1	yes	non-radial outward

tailed description of the cross-identification and the computation of the kinematic parameters see (Fromm et al. 2013a).

The jet in CTA 102 shows a bent structure and can be divided into four regions (see Fig. 4). The outermost region ($r > 7$ mas) consists of two components labeled as A1 and A2. These two features could be well traced and identified across the different epochs and are visible in the 5 GHz to 15 GHz observations. The calculated apparent speed for A1 is around $\beta_{\text{app}} = 9.4$ and $\beta_{\text{app}} = 8.7$ for component A2. The trajectory for A1 shows a non-radial inward motion which could be due the small pattern speed and/or projection effects, whereas A2 shows a clear radial outward motion. The linear back interpolation of the A2 trajectory leads to an ejection epoch around 1945.

Between $4 \text{ mas} < r < 7 \text{ mas}$, we parameterised the structure of the jet with three components, namely B1, B2, B3. This component triplet can be regarded as the most prominent structure in the jet of CTA 102 and is visible throughout our entire data set from 5 GHz to 43 GHz. All three features show a very small apparent speed ($0.8 < \beta_{\text{app}} < 1.4$) and the feature labeled as B2 could be described as a quasi-stationary feature within our model accuracy.

The region which spans the distance between $1 \text{ mas} < r < 3 \text{ mas}$ from the core is best described by 2 components labeled as D1 and D2 (see Fig. 5). Within this region, the aforementioned splitting of the components due the increased resolution occurs. Only in the 15 GHz observations a third Gaussian, labeled as D3 was needed to properly model the emission structure with this region. The component D1 was located at $r \sim 2.1$ and reveals a non-radial motion with an apparent speed of $\beta_{\text{app}} = 5.7$. The second feature, D2, is ejected around 1997 with an apparent speed of $\beta_{\text{app}} = 8.3$ and shows a clear radial outward motion.

The cross-identification of components in the core region ($r < 1 \text{ mas}$) was a difficult task due to the splitting of components and the ejection of new ones, connected to the flaring activity of the source. Therefore, we focused on the 43 GHz observations which provide the highest angular resolution. Based on these observations we identified four components labeled as C1, C2, C3 and C4. Only compo-

nents C1 and C2 show a clear radial outward motion with an apparent speed of $\beta_{\text{app}} \sim 12$ and were ejected from the radio core in 2005.1 and 2005.9. In Fig. 6 we show a vector motion map for the innermost components labeled as C1, C2, C3, and C4 obtained from the 43 GHz VLBI observations.

4.3 Jet structure

Besides the study of the kinematic properties of the jet, VLBI observations can be used to investigate the transversal jet structure. In order to extract the jet width from the observations we derived first the jet ridge line, i.e., the line connecting the local flux density maxima along the jet and approximated the transversal flux density profiles with a Gaussian (see, e.g., Fromm et al. 2013b; Pushkarev et al. 2009). For this analysis we stacked all VLBI images of a given frequency in order to reduce possible calibration uncertainties on the emission structure. Therefore, the obtained values could be regarded as the average jet ridge line and jet width. The de-convolved jet width, w , was obtained from the FWHM of the fitted Gaussian and the beam size transversal to the jet ridge line b_ϕ via the relation

$$w = \sqrt{\text{FWHM}^2 - b_\phi^2}. \quad (15)$$

The results of this analysis revealed a pinching jet, i.e., the jet shows regions where the jet cross-section increases (opening of the jet) and decreases (closing of the jet) with distance. As an example of the analysis we show in Fig. 7 the evolution of the de-convolved jet width, w , with distance along the jet obtained from the stacked 15 GHz observations. For $r > 0.5$ mas from the radio core we can resolve the transversal jet width. The jet is opening (increase in w with distance) until $r \sim 1.5$ mas with two different opening rates, visible by the different slope of w . The first clear closing of the jet, i.e., decrease of the jet width with distance along the jet, occurs between $1.5 \text{ mas} < r < 2.0 \text{ mas}$, and there are additional regions where the jet re-collimates, located between $3.5 \text{ mas} < r < 4.7 \text{ mas}$ and $5.5 \text{ mas} < r < 6.5 \text{ mas}$. The results obtained are in good agreement with

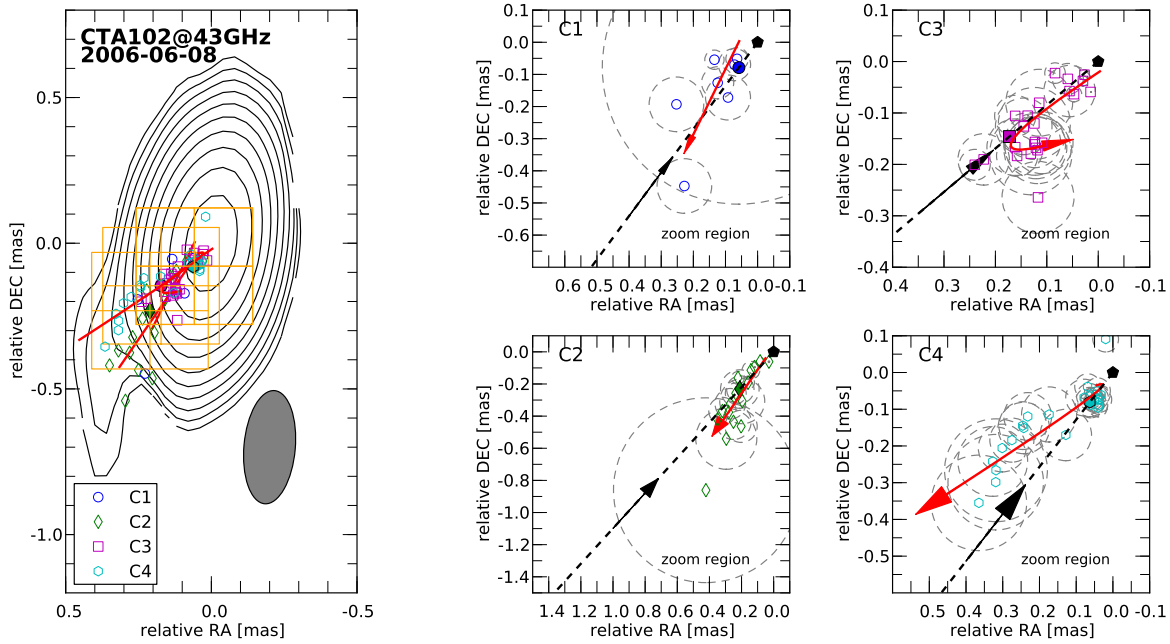


Fig. 6 Vector motion fits and position of the fitted component in the sky. *Left*: 43 GHz CLEAN VLBI map of the 2006 June observations of CTA 102. The lowest contour level is drawn at 10 times the off-source rms, and the contours increase with steps of 2. The observational beam is plotted in the bottom right corner. The open blue, green, magenta and cyan symbols indicate the position of the components labeled as C1, C2, C3, and C4. The filled symbol corresponds to the component position at the middle time, t_0 , and the red solid line to the trajectory of the feature. The orange squares show the zoom region. *Right*: zoom region for the individual components. The dashed grey circle are the components size (FWHM) and the dashed black line and black arrow correspond the direction to the core drawn from the position of the component at t_0 . The red solid line illustrates the trajectory of the component, and the direction of the component is indicated by the arrow.

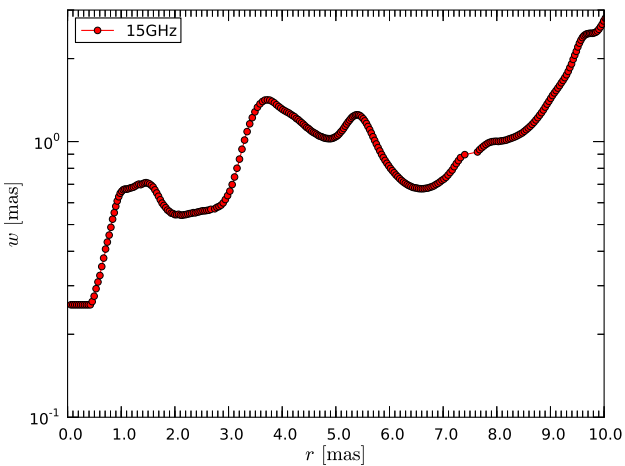


Fig. 7 The evolution of the de-convolved jet width along the jet obtained from stacked 15 GHz VLBI observations of CTA 102.

the evolution of the jet width with distance for the other frequencies involved in our data set (see Sect. 4 in Fromm et al. 2013b).

4.4 Spectral evolution

Simultaneous multi-frequency VLBI observations can be used to extract the temporal and spatial spectral evolution along the jet. Therefore, we have to stack the simultaneous

images at different frequencies. Since absolute position of the source is lost during the calibration of the data, we have to correct for the initial position. One of the most promising techniques if the source exhibits enough structure at all frequencies is 2D-cross-correlation. For the data on CTA 102 we used this technique to restore the initial position of the jet (for more details on the image alignment see Sect. 2.1 in Fromm et al. 2013b). After correcting for this opacity shift, we fitted a synchrotron self-absorbed spectrum or a power law to the spectrum at each pixel depending whether the turnover frequency is within the observed frequency range (here 2 GHz–86 GHz) or not.

Since the emission in the core region, $r < 1$ mas, is strongly affected by the variation of the underlying physical properties of the jet and observational limitations (e.g., resolution and convolution effects) we only used high frequency VLBI images with $\nu \geq 15$ GHz and fitted a power law to the spectrum at each pixel. The spatial and temporal variation of the spectral index along the jet for six different times is presented in Fig. 8. The spectrum is optically thick ($\alpha > 0$) for all epochs within $r < 0.2$ mas and optically thin for all epochs for $r > 0.4$ mas. The variation of the transition point from optically thick to optically thin and the variation absolute value of the spectral index, $|\alpha|$, reflects possible injection of new relativistic particles at the onset of the jet (see Sect. 5).

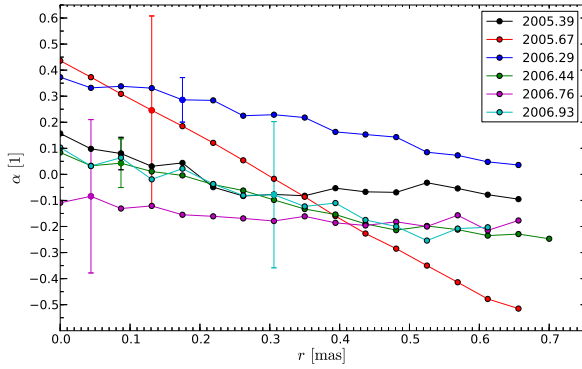


Fig. 8 The evolution of the spectral index, α , ($S_\nu \propto \nu^\alpha$) for $r < 1$ mas along the jet.

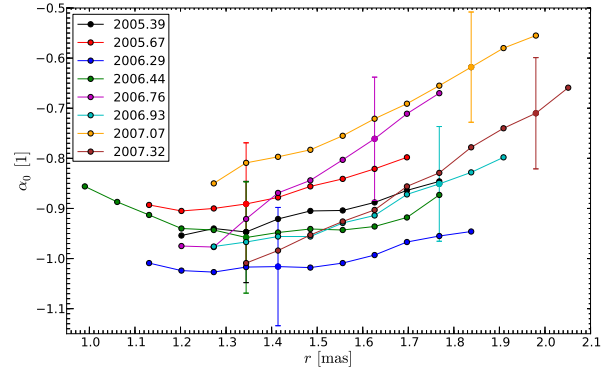


Fig. 11 The evolution of the optically thin spectral index, α_0 , for $1 \text{ mas} < r < 2 \text{ mas}$ along the jet.

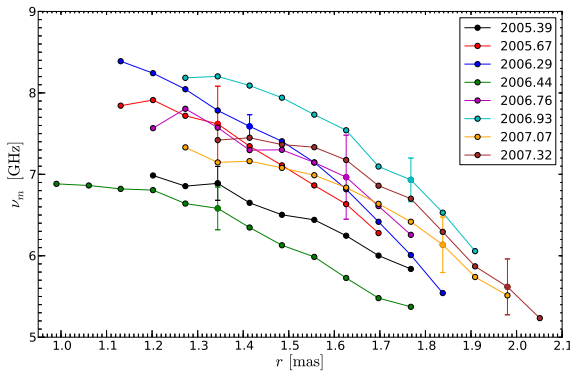


Fig. 9 The evolution of the turnover frequency, ν_m , for $1 \text{ mas} < r < 2 \text{ mas}$ along the jet.

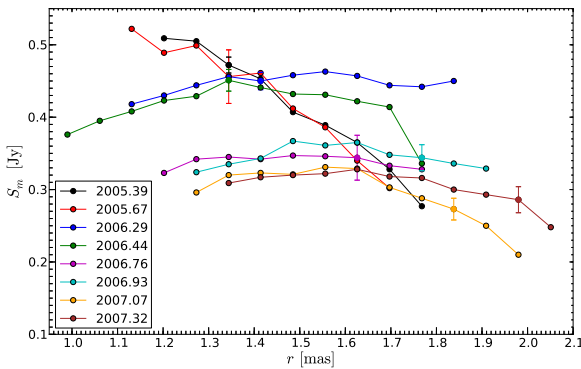


Fig. 10 The evolution of the turnover flux density, S_m , for $1 \text{ mas} < r < 2 \text{ mas}$ along the jet.

For the region between $1 \text{ mas} < r < 2 \text{ mas}$ the spectral turnover is within in our frequency range and therefore we fitted a synchrotron self-absorbed spectrum to the data (see Eq. 1). The variation in the turnover frequency, ν_m , the turnover flux density, S_m , and the optically thin spectral index, α_0 is plotted in Figs. 9–11. The turnover frequency is varying between $5 \text{ GHz} < \nu_m < 8.3 \text{ GHz}$ and the turnover flux density between $0.2 \text{ Jy} < S_m < 0.5 \text{ Jy}$.

Further downstream, the turnover frequency is outside of our frequency range and therefore, we fitted a power law

to the spectrum at each pixel. The spectrum is clearly optically thin, reflected by $\alpha < 0$ and shows strong variation along the jet axis. In Fig. 12 we present the variation of the spectral index along the jet axis for $r > 2 \text{ mas}$. The spectral index varies between $-1.3 < \alpha < -0.3$ and shows two local maxima, which reflect a possible re-acceleration of the relativistic electron distribution at these locations (see more in Sect. 5).

5 Discussion

The analysis of single-dish and VLBI observations shows indications for several stationary features in the jet of CTA 102. These stationary features can be interpreted as recollimation shocks. The formation of recollimation shocks can be described in the following way: The unbalance between the jet pressure and the pressure of the ambient medium at the jet nozzle leads to an opening of the jet. According to the conservation laws of hydrodynamics, this opening results in a decrease of the density, the pressure, and the magnetic field intensity in the jet. The finite speed of the sound waves in the jet is responsible for an over-expansion followed by a recollimation of the jet that gives rise to the formation of a shock. During this collimation

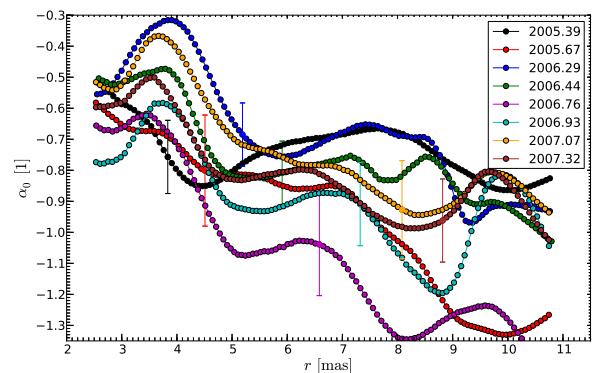


Fig. 12 The evolution of the spectral index, α , ($S_\nu \propto \nu^\alpha$) for $r > 2 \text{ mas}$ along the jet.

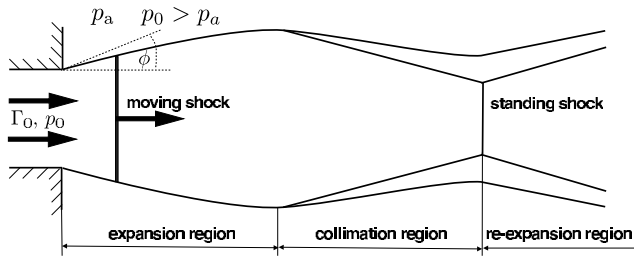


Fig. 13 Sketch of an over-pressured jet with indicated expansion and collimation regions (adopted from Daly & Marscher 1988).

process the jet radius decreases and the shock leads to an increase of the pressure, density, and magnetic field intensity. Again, the finite speed of the sound waves is responsible for an over-collimation of the jet. This interplay between over-expansion and over-collimation leads to the picture of a pinching flow, i.e., a continuous change of the width along the jet axis, in contrast to conical jets. The intrinsic physical parameters (pressure, density, and magnetic field) along a pinching jet show a sequence of local maxima and minima (Daly & Marscher 1988; Falle 1991). Therefore, the structure of the jet can be divided into expansion and collimation regions (see Fig. 13). The interaction between a re-collimation shock and a travelling shock can lead to an increase in the emission (Gómez et al. 1997). In the following we discuss the obtained results within the framework of an over-pressured jet.

5.1 The 2006 radio flare

The onset of flare was detected around 2005.6 with a turnover frequency of $\nu_m \approx 200$ GHz and a turnover flux density of $S_m \approx 3$ Jy. During the first 0.2 yr after the detection of the flare, the turnover flux density increased while the turnover frequency decreased (see Fig. 3), which reflects the characteristics of a Compton stage (i.e., inverse Compton losses are the main energy loss mechanism). Between 2005.8 and 2006.0, both the turnover flux density and the turnover frequency decreased, which can be interpreted as an adiabatic stage.

The application of the shock-in-jet model to the evolution of the turnover values between 2005.6 and 2006.0 revealed a jet opening index, $\rho = 0.6$, a purely toroidal magnetic field (indicated by $b = 1$), a spectral slope of $s = 2.1$ ($\alpha = -0.55$), and $d = 0.2$. The obtained jet opening index, $\rho > 0$, corresponds to an opening of the jet which should lead to an acceleration of the flow. If we assume that the viewing angle is constant within this region, the variation of the Doppler factor reflects the changes in the velocity of the plasma. Within the shock-in-jet model such an acceleration is given by $\rho d < 0$ ($D \propto r^{-\rho d}$). We obtained $D \propto r^{-0.12}$ which corresponds to a deceleration of the flow. However, this value is small and therefore comparable with a constant velocity (assuming a constant viewing angle). Since the turnover frequency within this time span (2005.6–2006.0) is larger than 43 GHz and due to the lim-

ited angular resolution, we could not detect the ejection of a new feature from the VLBI observations. However, the increase in the 43 GHz core flux density during this period was a clear indication for the presence of a perturbation (see bottom panel in Fig. 14).

Around 2006.1 we detected in the 43 GHz VLBI observations a new feature labeled as C2. A linear back-interpolation of the C2 trajectory to the 43 GHz radio core lead to an ejection epoch of 2005.9. Therefore, we could use the obtained velocity of the C2 component as an approximation of the shock wave velocity. The increase of the turnover flux density after 2006.0 can be interpreted by the interaction between the travelling shock wave and a re-collimation shock. Using the velocity of the C2 component $\mu = 0.25$ mas/yr we located the recollimation shock around 0.1 mas away from the core. We found indications for such a stationary component within the 43 GHz VLBI long-term monitoring of CTA 102 (see top panel in Fig. 14). At the location of the re-collimation shock, the density, the pressure and the magnetic field show a local maximum and the passage of the travelling shock wave through this region lead to an increase in the emission. From the modelling we obtained $\rho = 0.35$ which indicates a slower rate of jet expansion than in the previous region and the Doppler factor seems to be constant ($D \propto r^{0.035}$). The magnetic field within this region showed a contribution of a poloidal component which is reflected by $b = 1.35$, in contrast to the purely toroidal field within first expansion region.

After 2006.3 the travelling shock waves left the re-collimation region and entered an additional expansion region which lead to a decrease in the turnover flux density and the turnover frequency (see Fig. 3). This behaviour was supported by the obtained exponent for the evolution of the jet radius with distance, $\rho = 0.9$, and the acceleration of the flow (assuming a constant viewing angle) expressed by $D \propto r^{0.2}$. The decrease of the spectral slope from $s = 2.0$ to $s = 2.4$ reflected the ageing of the relativistic electron distribution by synchrotron cooling and adiabatic expansion. The obtained value for the evolution of the magnetic field increased from $b = 1.35$ to $b = 1.7$ which indicated a change in the geometry of the magnetic field from a purely toroidal one during the first 0.2 yr of the flare (or within the first expansion region) to a nearly poloidal one at the end of the flare (or in the second expansion region).

In Fig. 14 we show the correlation between the ejection of VLBI components at the radio core, the crossing of a possible re-collimation shock at $r \sim 0.1$ mas and the single dish light curves. The component labeled as C2 was ejected around 2005.9 with a speed of 0.25 mas/yr. This ejection epoch fits nicely to first peak in the 230 GHz light curve and the crossing of the stationary feature at $r \sim 0.1$ mas around 2006.4 corresponds to the peak in the 37 GHz light curve. Therefore, we can connect the ejection of the component C2 with travelling shock wave generated by the 2006 radio flare and its passage through the stationary feature at $r \sim 0.1$ mas with the second peak in the ν_m - S_m plane.

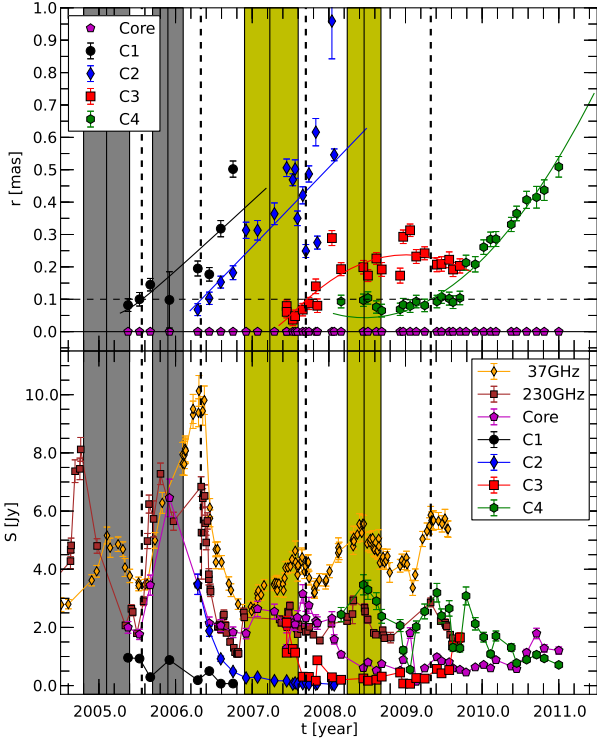


Fig. 14 Evolution of the component separation from the core and the flux density for the innermost components of CTA 102. *Top*: separation from the core and fitted trajectories for C1, C2, C3, and C4. The grey and yellow shaded areas correspond to the ejection epochs for C1, C2, C3, and C4, and the dashed line to the crossing of a possible stationary feature at $r \sim 0.1$ mas away from the core (dashed horizontal line). *Bottom*: flux density evolution of the components including the core and single-dish flux density measurements at 37 GHz and 230 GHz. For details see text.

5.2 Post 2006 radio flares in CTA 102

The light curve of CTA 102 showed additional flares after the main radio flare in 2006 (see Fig. 1). Using the 43 GHz VLBI observations we could identify two additional components labeled C3 and C4 which can be connected to these flares. As mentioned in Sect. 4.2, these two components show non-radial trajectories. Close to the core there are possible blending effect between components which could lead to miss-identification of the features. We separated these two components into stationary and travelling part and derived the ejection epoch. In Fig. 14 we indicate the possible ejection dates with the yellow areas and they correspond to the peaks in the 37 GHz light curve at 2007.2 and 2008.4 and the peaks around 2007.8 and 2009.4 to the possible interaction between the travelling shock waves and the recollimation shock at $r \sim 0.1$ mas.

5.3 Additional recollimation shocks

In addition to the recollimation shock at $r \sim 0.1$ mas, we found additional recollimation shocks located further downstream. The de-convolved jet width, w , showed several col-

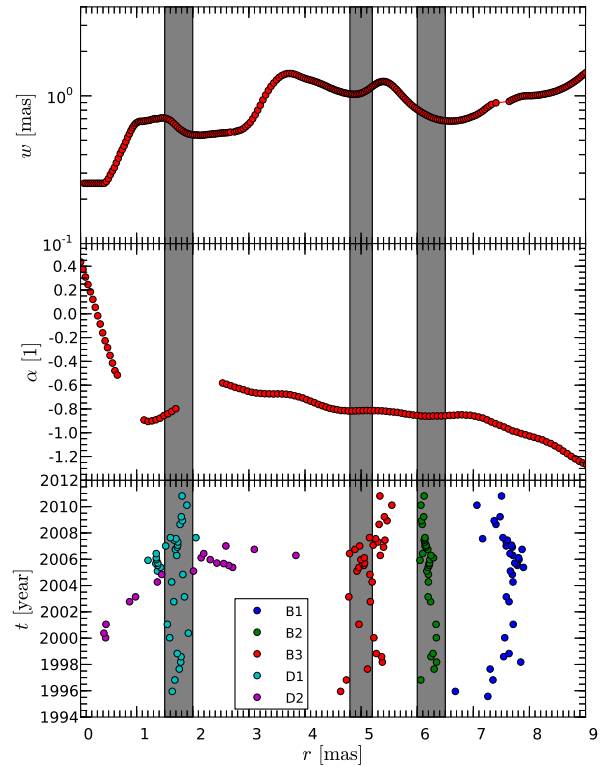


Fig. 15 Evolution of the jet width, w (*top*), the spectral index, α , (*middle*), and the cross-identified components along the jet (*bottom*). The grey shaded areas indicated possible locations of recollimation shocks (see text for more details).

limation regions at $r \sim 1.0$ mas, at $r \sim 5.0$ mas, and at $r \sim 6.0$ mas. Furthermore, we found indications for an increase in the spectral index, α , at these positions and they correspond to the location of quasi-stationary components (see Fig. 15). The closing of the jet and the increase of the spectral index are clear indications for the pressure unbalance in the jet. In the collimation regions the pressure, density and magnetic field increase which leads to a local enhancement in the emission and to an increase of the spectral index (see, e.g., Mimica et al. 2009). The increase in the spectral index and the mixing of the components at $r \sim 1.5$ mas could be indications for a second travelling shock–recollimation shock interaction in CTA 102.

6 Conclusion

We analysed the 2006 radio flare in the blazar CTA 102 using single-dish observations and VLBI observations. The spectral analysis of the single-dish light curves revealed a double peak structure in the turnover frequency–turnover flux density plane. This evolution cannot be explained by a simple shock-in-jet model. Therefore we included a possible travelling shock–recollimation shock interaction in the model. These recollimation shocks are common features in over-pressured jets (pressure unbalance between the jet and the ambient medium). Further evidence for a such a sce-

nario was obtained from the the analysis of the single and multi-frequency VLBI observations. The kinematic analysis revealed several features which were ejected during the flaring activity of the source and one could be connected to the 2006 radio flare. In addition, we obtained several stationary components which can be regarded as recollimation shocks. The location of these recollimation shocks corresponds nicely to local maxima in the spectral index and to local minima in the transversal jet width. The proposed scenario can be tested with high-resolution relativistic hydrodynamic simulations and connected non-thermal emission simulations can confirm or reject our scenario of shock-shock interaction.

Acknowledgements. C.M.F. was supported for this research through a stipend from the International Max Planck Research School (IMPRS) for Astronomy and Astrophysics at the Universities of Bonn and Cologne. Part of this work was supported by the COST Action MP0905 “Black Holes in a violent Universe”. C.M.F. thanks Eduardo Ros and Manel Perucho for fruitful discussions and collaboration during the last 5 years. This work is based on observations with the VLBA, which is operated by the NRAO, a facility of the NSF under cooperative agreement by Associated Universities Inc. This research made use of data from the MOJAVE database that is maintained by the MOJAVE team (Lister et al. 2009).

References

- Daly, R. A., & Marscher, A. P. 1988, *ApJ*, 334, 539
 Falle, S. A. E. G. 1991, *MNRAS*, 250, 581
 Fromm, C. M., Perucho, M., Ros, E., et al. 2011, *A&A*, 531, A95
 Fromm, C. M., Ros, E., Perucho, M., et al. 2013a, *A&A*, 551, A32
 Fromm, C. M., Ros, E., Perucho, M., et al. 2013b, *A&A*, 557, A105
 Gómez, J. L., Martí, J. M. A., Marscher, A. P., Ibanez, J. M. A., & Alberdi, A. 1997, *ApJ*, 482, L33
 Harris, D. E., & Roberts, J. A. 1960, *PASP*, 72, 237
 Homan, D. C., Ojha, R., Wardle, J. F. C., et al. 2001, *ApJ*, 549, 840
 Lister, M. L., Aller, H. D., Aller, M. F., et al. 2009, *AJ*, 137, 3718
 Marscher, A. P., & Gear, W. K. 1985, *ApJ*, 298, 114
 Marscher, A. P., Jorstad, S. G., D’Arcangelo, F. D., et al. 2008, *Nature*, 452, 966
 Marscher, A. P., Jorstad, S. G., Larionov, V. M., et al. 2010, *ApJ*, 710, L126
 Mimica, P., Aloy, M.-A., Agudo, I., et al. 2009, *ApJ*, 696, 1142
 Pushkarev, A. B., Kovalev, Y. Y., Lister, M. L., & Savolainen, T. 2009, *A&A*, 507, L33
 Schinzel, F. K., Lobanov, A. P., Taylor, G. B., et al. 2012, *A&A*, 537, 70
 Shepherd, M. C. 1997, *Astronomical Data Analysis Software and Systems VI*, 125, 77
 Spencer, R. E., McDowell, J. C., Charlesworth, M., et al. 1989, *MNRAS*, 240, 657
 Türler, M., Courvoisier, T. J.-L., & Paltani, S. 2000, *A&A*, 361, 850